Failure Analysis and Reliability Model Development for Microsystems-Enabled Photovoltaics

Benjamin B. Yang, Jose L. Cruz-Campa, Gaddi S. Haase, Edward I. Cole Jr., Paiboon Tangyunyong, Paul J. Resnick, Alice C. Kilgo, Murat Okandan, Gregory N. Nielson

Sandia National Laboratories, Albuquerque, NM, 87185, USA

***Abstract* — Microsystems-enabled photovoltaics (MEPV) has great potential to meet increasing demands for light-weight, photovoltaic solutions with high power density and efficiency. This paper describes current efforts to build a reliability model for MEPVs as well as the development of failure analysis techniques to localize and characterize failed or underperforming cells. Defect localization methods such as electroluminescence under forward and reverse bias, as well as optical beam induced current using wavelengths above and below the device band gap, are presented. Current results also show that MEPV has good resilience against degradation caused by reverse bias stresses.**

***Index Terms* —photovoltaic cells, solar energy, reliability, failure analysis, thin film devices, silicon**

I. INTRODUCTION

Many applications of photovoltaics, such as those for space and portable devices, have a strong need for light-weight, flexible, and efficient solutions with a high specific power. Microsystems-enabled photovoltaics (MEPV) have great potential to satisfy these requirements. The MEPV approach utilizes microfabrication techniques to create arrays of thin hexagonal solar cells that are 250 μm to 1 mm in diameter and 14 μm to 20 μm in thickness [1]. These cells can be assembled onto flexible substrates and interconnected to produce arrays with high power density [2].

The novel fabrication and packaging techniques to create MEPV arrays result in the need for a new model for reliability prediction. In addition, the microfabrication origin of MEPV results in opportunities to utilize microelectronic failure analysis techniques. This paper describes the defect localization techniques that were applied to MEPV, and demonstrates its robustness towards reverse bias stress.

Section II provides an overview on the construction of MEPV. Section III introduces the failure analysis techniques used in this study and provides examples of successful application of these methods for defect localization. Section IV describes a study where significant degradation was induced in an MEPV device after extreme reverse bias stress. Section V continues to examine reverse bias degradation in MEPV by subjecting a device to 600 hours of reverse bias stress at -50 V and found a small amount of leakage current increase. Section VI summarizes and concludes the paper.

II. MEPV OVERVIEW

Fig. 1 shows an optical image of a 720 μm MEPV cell. The left half of the cell, labeled "p-type" has circular islands that are doped p-type. Similarly, the n-type side has circular islands with n-type doping. Visible in the picture are small etch release holes that facilitate the release of the device from the original silicon wafer as well as electroplated copper pillars with solder that connect the device to the final substrate. A sketch of the cross section along the purple dashed line is shown in Fig. 2.

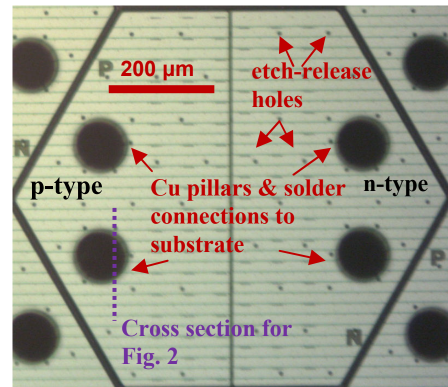

Fig. 1. Optical image of a 720 μm cell. The picture shows the metal layer that connects the p-doped (left half) and n-doped (right half) regions. Also visible are etch release holes and electroplated copper pillars with solder that connect the device to the final substrate. The purple line indicates the cross-sectional area that the sketch in Fig. 2 represents.

MEPV cells are initially fabricated on crystalline silicon wafers. The cross-sectional sketch of a p-type portion of an MEPV cell is shown in Fig. 2 to better illustrate the fabrication steps. The orientation in the figure is that of the final configuration (metal 1 side down, silicon side up) and should be initially rotated 180° to represent the device prior to release from the silicon wafer.

First, circular p-type and n-type areas are created using ion implantation. A metal 1 layer is deposited along with contacts that connect it to the doped regions. Metal pillars are then electroplated to the metal 1 layer and solder is applied to the tips. The MEPV cells are then released from the silicon substrate through an etch release step. The cells are

reassembled, metal-side down as shown in Fig. 2, on the desired final rigid or flexible substrate to produce a honeycomb-like array pattern. Metal lines deposited on the substrate determine the final electrical configuration, which can be customized to fit the voltage and current requirements of the specific application.

After release, the original silicon wafer can be reused to fabricate more MEPV cells, resulting in material cost savings. The small size and thinness of the cell enables efficient carrier collection and reduces the number of defects [1].

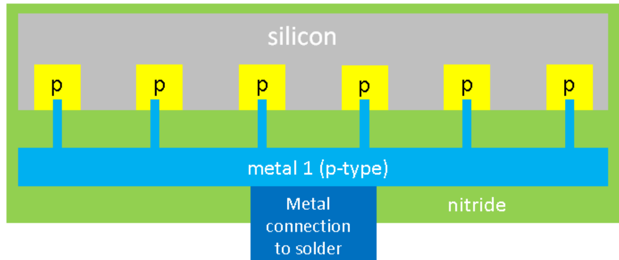

Fig. 2. Cross sectional sketch of an MEPV p-type region. Circular islands of p-doped silicon are connected to metal 1 by contacts. Electroplated pillars and solder, visible in Fig. 1, connect the metal 1 to the substrate. A nitride passivation layer surrounds the MEPV and also functions as an antireflection layer.

III. Failure Analysis Techniques and Results

The failure analysis techniques utilized in this paper include electrical characterization, electroluminescence (EL), and optical beam induced current (OBIC). The EL image consists of light emission collected from the device under forward bias, and is used to evaluate the relative performance of each cell [3]. In addition, EL under reverse bias is used to localize the source of significant leakage currents.

Fig. 3 shows an example of a forward biased EL image. The hexagonal photovoltaic cells in the image are 720 µm in diameter. Each horizontal row in the cell is connected in parallel and the rows are connected in series. The relative brightness of each row is related to the number of functioning cells in that row. EL is able to identify nonfunctioning cells as well as partially functioning ones. Examples of both situations are represented in Fig. 4. Under forward bias, all functioning cells emit light. Non-functioning cells do not appear in the image. If the cell has damaged regions, those areas can also be identified in the EL image.

OBIC uses a raster-scanning laser stimulus to generate currents in the device [4]. Low-noise amplification is performed on the induced signal to form an image. Fig. 4 provides a schematic of the electrical configuration of OBIC. When the laser stimulus has sufficient photon energy to generate electron-hole pairs, above-band-gap OBIC can used to evaluate cell performance and complements EL by providing additional information on localized efficiency in an individual cell. We use a laser wavelength of 543 nm for this mode of operation.

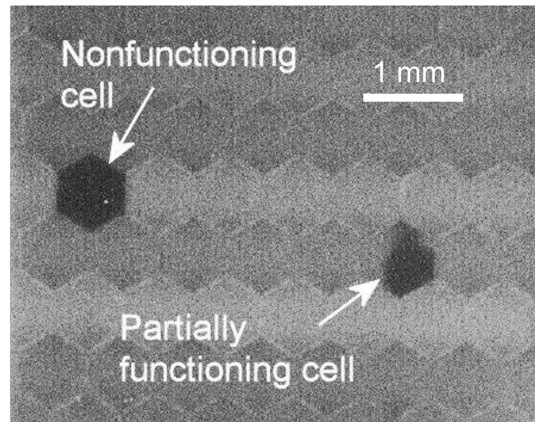

Fig. 3. Electroluminescence is used to evaluate relative efficiency of MEPV arrays. This figure shows an example of a non-functioning cell and a partially functioning one. Certain cells have area defects that limit performance.

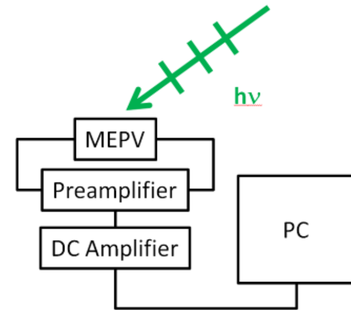

Fig. 4. A schematic of the OBIC technique. A laser with photon energy either above or below the material band gap is raster scanned across the device. Electron-hole pairs are generated if laser photon has energy above the band gap of silicon. If the laser photon energy is below the band gap, localized heating occurs. The resulting current is amplified and sent to the PC. The OBIC image is formed by plotting the DC amplifier output as a function of the laser position.

Fig. 5 shows an example where OBIC is used to determine localized efficiency within an individual MEPV cell. The right half of the cell is darker than the left half in the OBIC image. The contrast difference suggests a possible carrier collection issue with the right half of the cell. This non-uniform performance was not apparent under EL, further demonstrating the complementary nature of the two techniques.

Alternatively, below-band-gap OBIC can be used to provide additional device information. When the laser photon energy is below the device band gap, no electron-hole pairs are generated and localized heating occurs. In interface regions between materials, this localized heating generates currents that are amplified to form the OBIC image. This configuration

can be used to test the electrical contact and connectivity of the device separately from its ability to generate carriers.

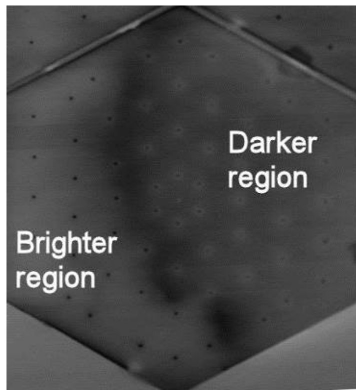

Fig. 5. OBIC image using an above-band-gap laser stimulus provides additional fidelity on the regional performance on a single MEPV cell. The darker half on the right indicates a possible carrier generation or collection issue.

We use a laser wavelength of 1340 nm to perform below-band-gap OBIC. Fig. 6 is an OBIC image containing both a working MEPV cell and a portion of a nonworking one. The electrical contacts that connect the silicon to the metal layer are visible if the cell is functioning. These contacts are not visible in the nonworking cell. Note that the OBIC image has contrast changes at the etch-release holes and the edges of the MEPV cell. This contrast is due to the temperature gradient induced by the laser across material interfaces. Through this mechanism, we see that the etch release holes are still visible in the nonfunctioning cell, suggesting that it is still electrically connected with the array. The failure mechanism could be related to the contacts between the silicon and metal layer. Further defect localization is necessary before subsequent destructive analysis to determine the root cause.

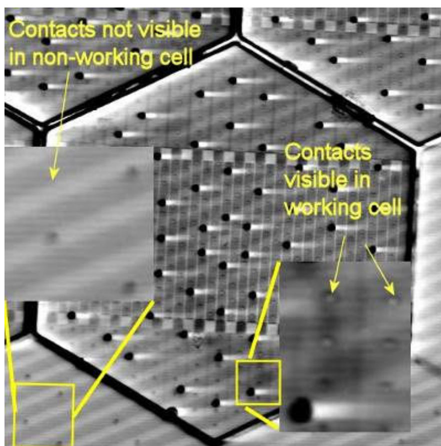

Fig. 6. 1340 nm wavelength OBIC enables the evaluation of the contacts between the silicon and metal layer. These contacts are shown as smaller dots that are not visible in the neighboring, nonfunctioning cells.

In addition to analysis through EL and OBIC, mechanically polished cross sections are analyzed to determine the quality of the electrical connection between the solar cell and the metal trace lines that connect them to each other. Fig. 7 illustrates two features of interest: voids in the solder connection and absorption of the metal trace lines into the solder. The voids could lead to increased series resistance or poor connection between the cell and the metal trace. Further analysis with scanning electron microscopy shows that the metal trace is thinner in regions in contact with the solder where it is potentially consumed due to the soldering process temperature. Both the voids and the decreased thickness in metal traces are present in functioning cells. Additional cross sections of samples that have experienced temperature cycling will provide more insight into the long-term effects of these defects.

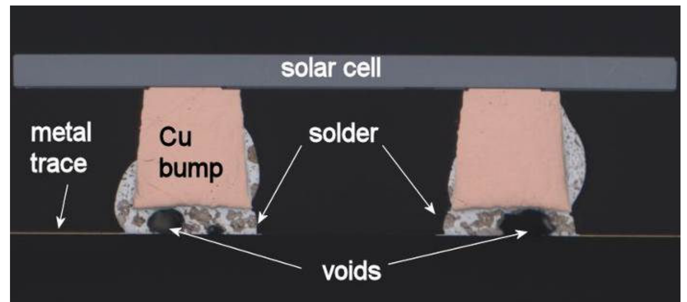

Fig. 7. Mechanical polishing and bright field optical microscopy has been used to evaluate the quality of the solder connection between the copper legs and the gold lines. Voids such as the one shown here could be a source for increased series resistance.

IV. Reverse-Bias Breakdown Defect Localization

Reverse bias stress occurs in photovoltaic cells when a module experiences partial shading, and is a source of degradation in photovoltaic modules [5]. We expect the MEPV to have good resistance towards reverse bias stress because the p-type and n-type regions are separated by a region of intrinsic silicon (a p-i-n device).

First, we present results of a MEPV device subjected to extreme reverse bias stress until there was a significant increase (100×) in leakage current. Breakdown did not occur until reverse bias stress exceeded -75 volts (V). Fig. 8 shows the reverse bias current-voltage (I-V) plot of 28 cells in parallel and illustrates the effect of extreme reverse bias stress. After 11 reverse bias voltage sweeps from 0V to -80V lasting approximately 10 seconds each, the leakage current begins to increase dramatically, especially at the lower voltages. The two IV-curves remain similar beyond -74V, suggesting that the source of leakage currents at extremely high voltages is not significantly affected by the new failure.

Further analysis of the sample in Fig. 8 shows that the effects of reverse bias stress are localized. Fig. 9 shows a

portion of the MEPV array forward biased EL image. The cell on the far right has a nonfunctioning region that is not emitting light.

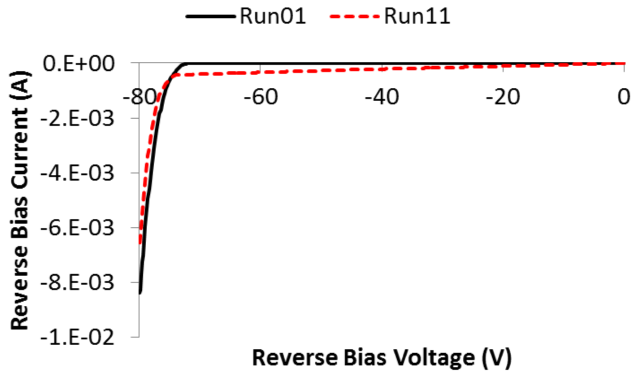

Fig. 8. Current-voltage curves before and after reverse bias stress. Each voltage sweep takes approximately 10 seconds. Breakdown occurs at approximately -75 V. We can see that current leakage is aggravated after repeated voltage stress.

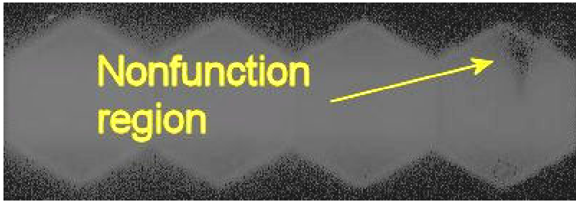

Fig. 9. Electroluminescence image of the MEPV cells measured in Fig. 8 after reverse bias stress. The cell on the far right has a non-functioning region.

This potential-induced defect was further localized by taking an EL image of the MEPV array under reverse (instead of forward) bias. Prior to the voltage stress, the MEPV array produced no detectable light emission under reverse bias. The post-stress reverse bias EL image of the cell of interest is shown in Fig. 10. In order to display the location of the defect, the optical emission is converted to a green (false) color and overlaid on top of a bright-field image of the cell.

The EL signal suggests a current-induced dislocation path. The reverse bias light emission has higher intensity than the forward bias MEPV EL signal, suggesting a different photon generation mechanism. One possibility is that the photons are generated by microplasma that is characteristic of avalanche breakdown [6]. The small, discrete, and localized nature of the light emission also supports this suggested mechanism.

V. Reverse-Bias Degradation Results

The subsequent study presented in this section focuses on lower reverse bias voltage stresses applied for longer periods of time for the purposes of building a reliability model for potential-induced degradation. Fig. 11 shows 300 reverse bias IV measurements, taken every two hours over the course of 600 hours of reverse bias stress at -50V. The device under test had 34 MEPV cells connected in parallel. The color transition from blue to red identifies the relative order of each IV sweep, with blue being the initial measurements and red being the last ones. The divisions on the left side of the plot provide estimations on the amount of stress applied prior to a given IV measurement.

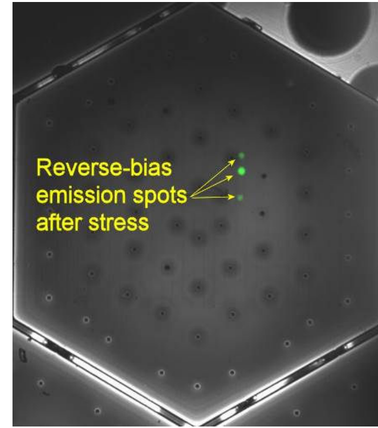

Fig. 10. Electroluminescence imaging of the MEPV cell under reverse bias shows three local defects that are the source of the leakage current.

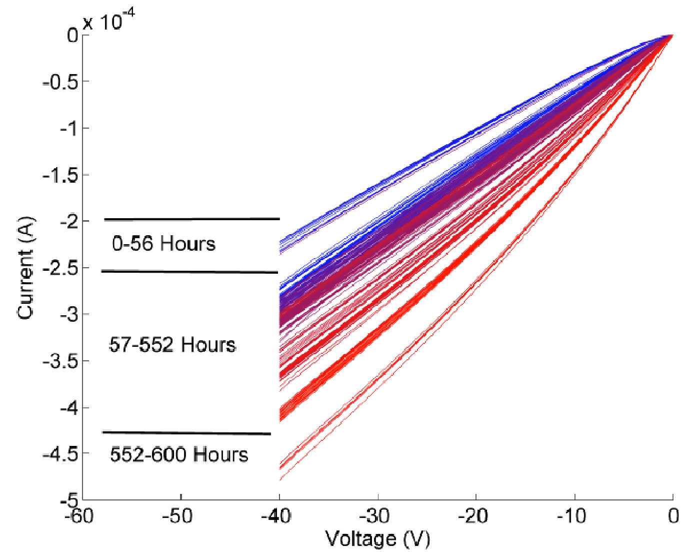

Fig. 11. Reverse bias IV sweeps taken in two-hour intervals during a 600-hour reverse bias stress test at -50 V. The line color transition of from blue to red indicates the relative order of the IV sweeps, with red being the last measurement. The three regions in the plot show the duration of reverse bias stress that occurred prior to the IV sweeps in the indicated area. We see that while the reverse bias current doubled during 600 hours of stress, the overall leakage is still moderate.

At the end of 600 hours of reverse bias stress, the current leakage roughly doubled but still remained at an acceptable amount of approximately -15 µA per cell at -40V. The transition to increased leakage current was gradual and continuous compared to the forward bias results, which are plotted separately in Fig. 12.

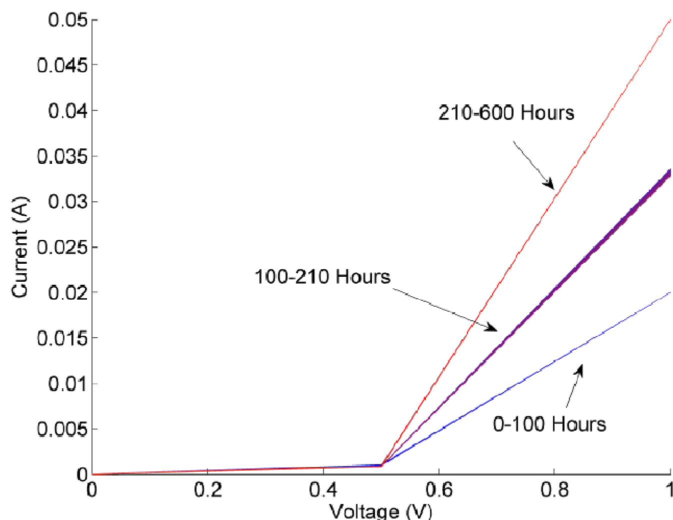

Fig. 12. Forward bias IV sweeps taken in two-hour intervals during a 600-hour reverse bias stress test at -50 V. Unlike the continuous, steady increase of leakage current in the reverse bias IV curves of Fig. 11, the forward bias current increase took place in two discrete transitions. This behavior suggests that two MEPV cells were damaged, one at approximately hour 100, the other at approximately hour 210.

Unlike the reverse bias stress, the forward bias IV curves exhibited very discrete increases in current for a given voltage. These changes occurred approximately after 100 hours and 210 hours of stressing. These sharp changes suggest two breakdown events that increased the amount of current flow through the damaged device.

A post-stress, forward bias EL examination was able to identify two MEPV cells with damaged regions. Fig. 13 shows a forward bias EL image of one of these cells where the damaged area is apparent. Subsequent destructive failure analysis is needed to determine the exact nature of the breakdown.

Unlike the damaged sample in Section IV, there was insufficient leakage to generate a detectable reverse bias EL image. The lack of strong, localized emission under reverse bias suggests that the avalanche breakdown failure mechanism observed in the previous section has not yet occurred on this sample. Therefore, when developing reliability data for an MEPV system, it is important not to overstress the device at voltages significantly beyond the partial shading reverse bias voltages expected for the specific application and operating conditions. Overstressing could lead to new failure modes such as the observed avalanche breakdown in Section IV that may not occur during actual operation of the system.

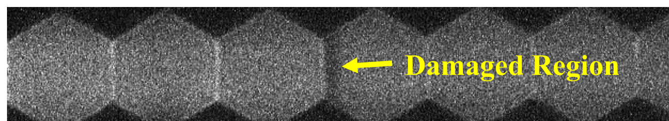

Fig. 13. Forward bias EL image of one of the two damaged MEPV cells in the post-stress device studied in Fig. 11 and 12. The darker region labeled localizes the defect to the left edge of the cell shown.

VI. Conclusions

Current research to explore the reliability of MEPV devices utilizes tools such as electrical characterization, EL, multi-wavelength OBIC, and physical failure analysis to establish an effective set of failure analysis techniques for the technology. These methods are used to characterize MEPV devices and localized failure sites. EL and above-band-gap OBIC were demonstrated as methods to evaluate MEPV cell efficiency. Below-band-gap OBIC was shown to be an effective method to separately verify electrical connectivity of an MEPV cell.

We have also demonstrated good resilience to reverse bias voltage degradation. We found significant increases in leakage current, possibly due to avalanche breakdown, at voltage stresses exceeding -80V. Minor increases in leakage current without the behavior of avalanche breakdown were observed after 600 hours of voltage stress at -50V. The evolution of the forward bias IV curves correlated to the number of new defects, which was later verified using forward bias EL. Additional tests will enable development of a reliability model for reverse bias stress. The inclusion of additional stress testing such as temperature cycling and damp heat will lead to a comprehensive model to predict reliability. Failure analysis of accelerated testing samples will provide insight on how to further enhance the reliability of MEPV.

VII. Acknowledgements

Sandia National Laboratories is a multi-program laboratory managed and operated by Sandia Corporation, a wholly owned subsidiary of Lockheed Martin Corporation, for the U.S. Department of Energy's National Nuclear Security Administration under contract DE-AC04-94AL85000.

References

[1] G. N. Nielson, M. Okandan, J. L. Cruz-Campa, A. L. Lentine, W. C. Sweatt, V. P. Gupta, and J. S. Nelson, “Leveraging scale effects to create next-generation photovoltaic systems through micro- and nanotechnologies,” Proceedings of SPIE, vol. 8373, pp. 837317–837317, May 2012.

[2] J. L. Cruz-Campa, G. N. Nielson, P. J. Resnick, C. A. Sanchez, P. J. Clews, M. Okandan, T. Friedmann, and V. P. Gupta, “Ultrathin Flexible Crystalline Silicon: Microsystems-Enabled Photovoltaics,” IEEE Journal of Photovoltaics, vol. 1, no. 1, pp. 3 –8, Jul. 2011.

[3] R. Ross, ed., Microelectronic Failure Analysis Desk Reference, 6th Edition, ASM International, Materials Park, Ohio, 1999.
[4] E. I. Cole, P. Tangyunyong, D. L. Barton, “Backside localization of open and shorted IC interconnections,” Proceedings of IRPS, 1998.
[5] G. B. Alers, J. Zhou, C. Deline, P. Hacke, and S. R. Kurtz, “Degradation of individual cells in a module measured with differential IV analysis,” Progress in Photovoltaics: Research and Applications, vol. 19, no. 8, pp. 977–982, 2011.
[6] D. V. Kerns, K. Arora, S. Kurinec, and W. Power, “Si diode under avalanche breakdown as a light emitting source for VLSI optical interconnect,” in the Twenty-First Southeastern Symposium on System Theory, 1989. Proceedings, 1989, pp. 677–680.